RADAR IMAGING MECHANISM OF UNDERWATER WRECKS IN COASTAL WATERS WITH STRONG TIDAL CURRENTS

Ingo Hennings

IFM-GEOMAR Leibniz-Institut für Meereswissenschaften an der Universität Kiel, 24148 Kiel, Germany; ihennings@ifm-geomar.de

ABSTRACT

The radar imaging mechanism of underwater wrecks is investigated applying the quasi-specular scattering theory of shallow sea bottom topography considering both, the gravity as well as the capillary wave ranges. Wreck marks, e.g. sand ribbons, arising at the wreck of the motor vessel (M.V.) Birkenfels in the southern North Sea are analyzed. The formation of wreck marks at the sea bed and the manifestation of radar signatures at the water surface are caused by a vortex pair or helical flow cells triggered by unidirectional tidal current flow interacting with the wreck. The calculated strain rate of the imaging theory has the same order of magnitude as those obtained for other bed forms such as marine sand waves. This implies that the responsible hydrodynamic interaction produce radar signatures of submarine wrecks and make them visible at the sea surface. Wreck marks manifesting as sand ribbons at the sea bed as well as radar signatures of wrecks at the water surface are corresponding indicators of the local (tidal) current direction.

INTRODUCTION

Wreck search and other investigations of underwater obstacles are special applications of hydrographical surveying. Its goal is primarily the determination of the location with the exact positioning and surveying of the shallowest water depth above wrecks and objects on the sea bed. To ensure the safety of shipping these data are indicated as symbols and abbreviations in nautical charts or in Electronic Navigational Chart (ENC) data of Electronic Chart Display and Information Systems (ECDIS). More information on wreck search, wreck positions in the North Sea and Baltic Sea, historical and modern wreck search methods can be found under http://www.bsh.de. On the other hand, a sea bed area of a raised number of shipwrecks can be an indicator for the occurrence of abnormal waves such as freak or rogue waves (i). A large number of ship accidents have occurred in crossing sea conditions (ii).

When ship and deep-drought routes are planned it is necessary to investigate all wrecks in the vicinity of the route and to guarantee sufficient water depth above the wrecks. Displacements of ship wrecks and the genesis of scour hollows according to bottom currents can occur. It was shown (iii) that the head and tail aprons of sand waves manifesting to the north and south ends of sand banks are similar to wreck marks from a wreck lying sub-parallel to the regional sand transport direction. Sand in transit is slowed by the obstacle, swept along the wreck and then passes on into a plume of sand waves from its down-stream end. A wreck extending some 15 m above the sea bed in the vicinity of Sandettie Bank in the southern North Sea was undetected for 35 years (iv).

Under certain conditions radar signatures of the sea surface show not only underwater bottom topography features and other oceanographic and meteorological phenomena in shallow waters but also the position of submarine obstacles such as wrecks. A curved wake of a submerged wreck imaged on a radar scene was identified (v). The wake extends more than 4 km along the changing direction of the tidal flow. Several radar signatures corresponding with positions of submarine wrecks on sea charts in the Strait of Dover and the Southern Bight of the North Sea were analyzed (vi). Radar signatures of wrecks are imaged like comet marks on side-scan sonar records. Comet marks are defined as obstacle-induced, long erosive strips occurring on current-affected sea bottoms (vii). These features are mainly observed on side-scan sonar records due to acoustical back-

scattering contrast between the erosive zone and the surrounding sea bed. Radar signatures of underwater wrecks can also be compared with a turbulent ship wake of reduced radar backscatter, i.e. imaged as a dark feature, with one edge of enhanced radar backscatter, i.e. imaged as a bright feature. The bright edge is observed on that side of the wake from which the wind is blowing, the luff side of the wind direction. This is an area of intense water surface roughness. Short water waves are decelerated if they reach the turbulent wake region which is induced by the hull and propeller of the ship.

However, the full details of flow patterns around an obstacle are still unknown, even for unidirectional currents (viii). It has been assumed that the vortex created in front of an obstacle curls around it in a horseshoe shape. In some cases the horseshoe vortex system extends downstream as two helical eddies. The pattern of a secondary flow behind a spherical obstacle was discussed (vii). It has been found that this pattern should probably be interpreted as a pair of oppositely rotating spiral vortices. A new process-based model for wreck site formation was published (ix) and the current knowledge of scour at fully submerged structures under steady and oscillatory flow regimes has been reviewed (x).

This paper has the goal to discuss the formation of wreck marks or sand ribbons at the sea bed and the associated manifestation of radar signatures at the water surface caused by a vortex pair or helical flow cells triggered by unidirectional tidal current flow interacting with a wreck. In the second section data of the wreck of the motor vessel (M.V.) Birkenfels are described and analyzed. The proposed radar imaging theory of underwater wrecks is presented in the third section. Finally, the last section contains the discussion and conclusions.

METHODS

Birkenfels wreck data

On 7 April 1966 the German M.V. Birkenfels was on voyage from Bremen, Germany, to Khorramschar, Persian Gulf, with 8750 tons steel and general cargo on board. Around noon, in dense fog, the heavy lift ship came in collision with the German M.V. Marie Luise Bolten (15395 GRT) about one nautical mile southerly of Noord Hinder lightship in the southern North Sea and sunk. All crew members were rescued by M.V. Marie Luise Bolten and transferred to Rotterdam in the Netherlands. The simplified bathymetric chart of the West-, Noord-, and Oost Hinder Banks and the position of the M.V. Birkenfels wreck marked by the capital letter B in the vicinity of lightship Noord Hinder in the southern North Sea are shown in Figure 1. The bold black frame indicates the sea area imaged as the radar scene shown in Fig. 4 which covers parts of the West-, Noord-, and Oost Hinder Banks and shows also the wreck position. The shallowest water depth is about 8 m above the crests of the banks and in the swales between the tidal current ridges the maximum water depth is 46 m. The inset of Fig. 1 is a picture of the wreck buoy located westerly of the M.V. Birkenfels wreck position. At the time of the foundering of the M.V. Birkenfels only few prescribed shipping channels through the mine dispersed waters of the North Sea have been opened since the end of the Second World War. Between 1959 and 1964 a total of 1552 ships, an average of 300 ships per year, collided in the sea area of the German Bight and the English Channel. As the M.V. Birkenfels, many of them sunk. To demonstrate the shape and size of the wreck, a picture of M.V. Birkenfels before sinking on 7 April 1966, is shown in Figure 2 (http://www.ddg-hansa.de). General data of M.V. Birkenfels, the position, and the water depth of the wreck are listed in Table 1.

Figures 3a-d show the Kongsberg-Simrad EM1002 multi-beam echo sounder images of the M.V. Birkenfels wreck at different view angles acquired during the survey on 10 July 2001 from on board the Belgium research vessel (R.V.) Belgica. For more information the reader is referred to the Federal Public Service Economy, SMEs, independent Professions and Energy Service Continental shelf, Belgium, and http://www.mumm.ac.be. The EM1002 multi-beam echo sounder has frequencies of 93 kHz and 98 kHz, 111 acoustic beams are generated simultaneously up to ten times a second, and the system has a range between 2 m and 1000 m. The transducer has been

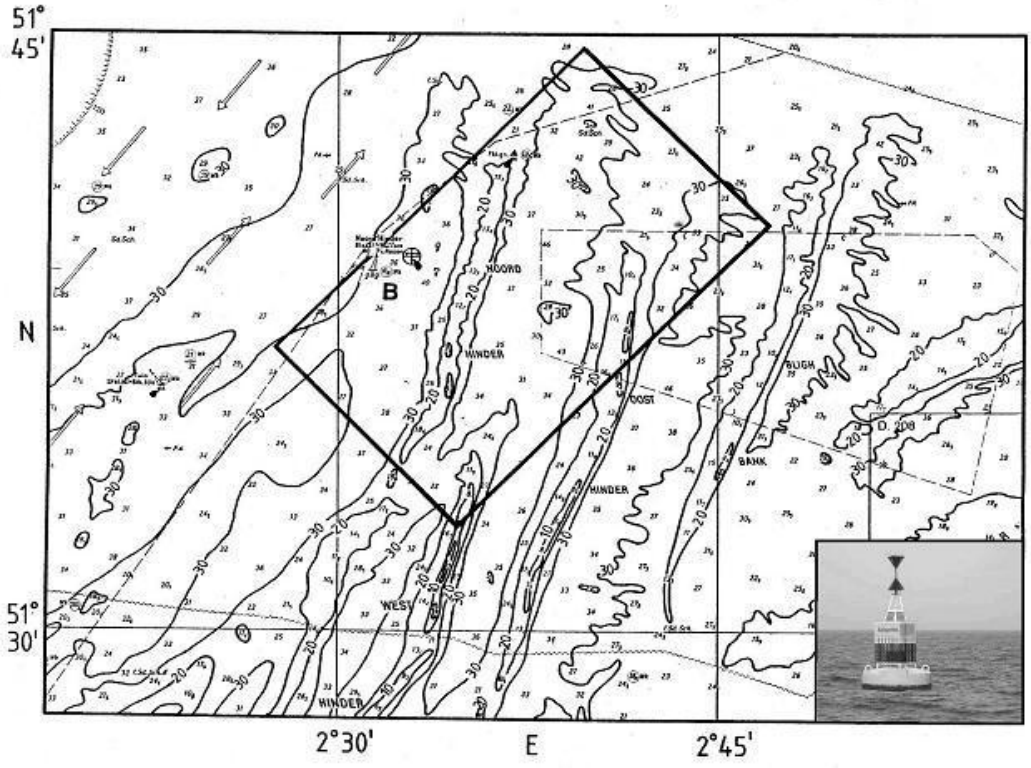

Figure 1: Simplified bathymetric chart of the West-, Noord-, and Oost Hinder Banks in the southern North Sea also imaged as radar signatures in Fig. 4. The area of the radar image shown in Fig. 4 is indicated by the bold black frame. The position of the M.V. Birkenfels wreck is marked by the capital letter B in the vicinity of lightship Noord Hinder. The inset shows a picture of the wreck buoy located westerly of the M.V. Birkenfels wreck position.

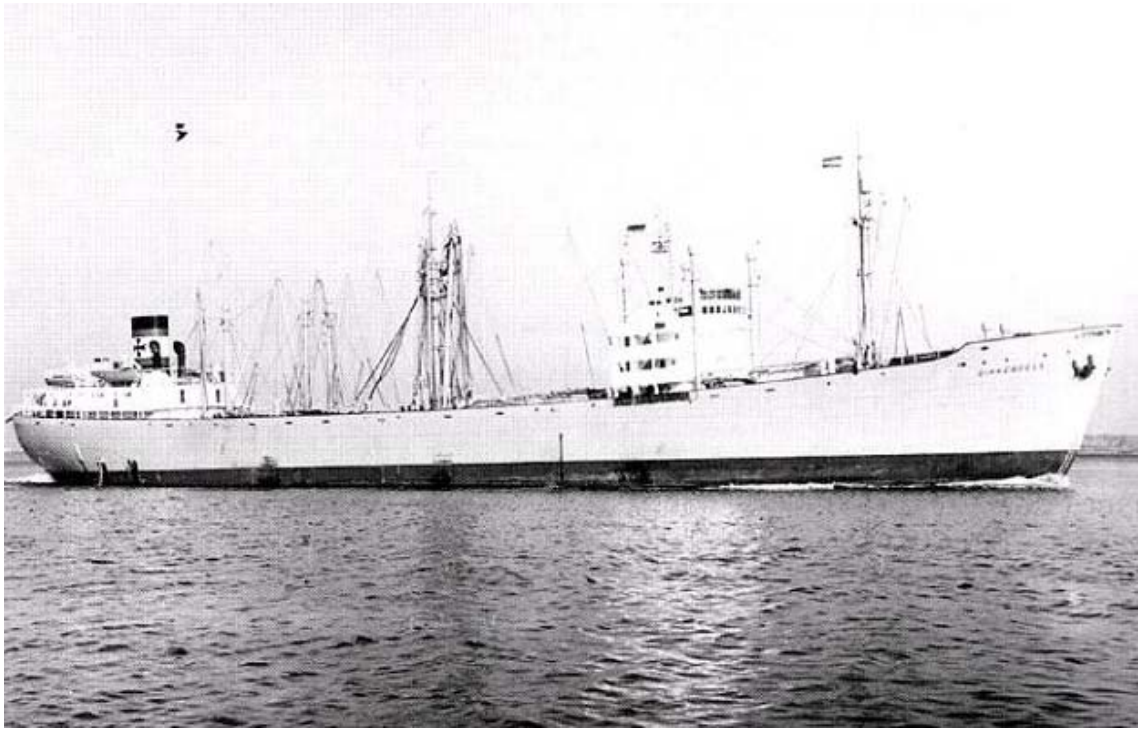

*Figure 2: Picture of M.V. Birkenfels before sinking on 7 April 1966 (*http://www.ddg-hansa.de*).*

Table 1: General data of M.V. Birkenfels, the position, and the water depth of the wreck.

nationality	German
owner	Deutsche Dampfschifffahrtsgesellschaft (DDG) Hansa, Bremen
type of ship	cargo ship
propulsion	motor vessel
deadweight carrying capacity (tdw)	10869
gross register tons (GRT)	6974
net register tons (NRT)	3982
length over all (LOA)	156.1 m
length between perpendiculars	146.0 m
length according register and measurement certificate	140.3 m
beam	18.68 m
draught	8.06 m
moulded depth (shelter decker)	9.20 m
horse power (HP)	3820
engine	MAN
speed	12.0 kn
crew	43
passengers	6
building year	1951
building yard	A.G. Weser Seebeck, Bremerhaven
yard number	696
heavy cargo gear	165 t
cause lost	collision
date lost	07.04.1966
position of wreck	$51^0 39.0'$ N, $2^0 31.9'$ E
water depth	36 m

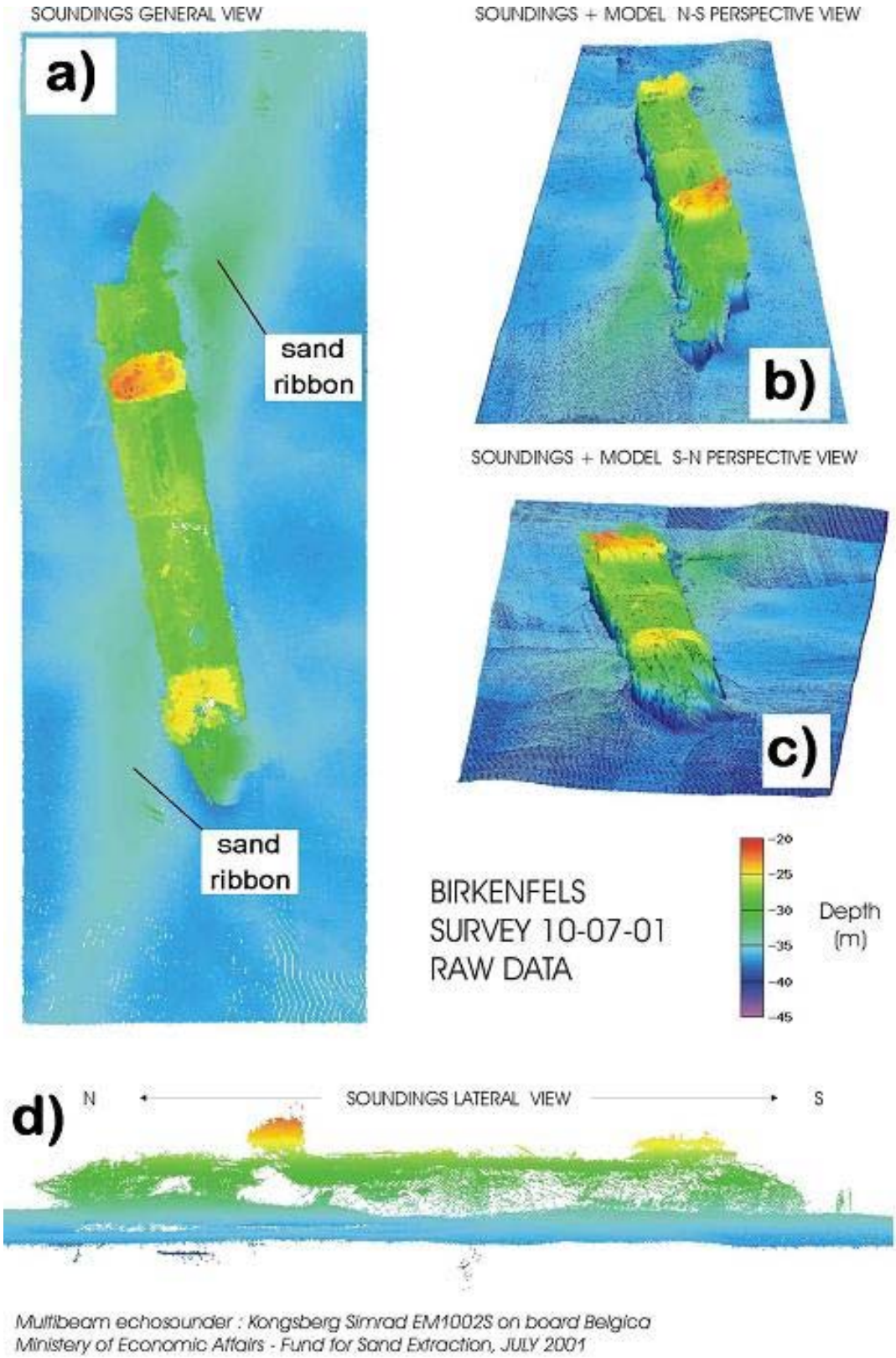

Figure 3: Kongsberg-Simrad EM1002 multi-beam echo sounder images of the M.V. Birkenfels wreck acquired during the survey on 10 July 2001 from on board the Belgium research vessel (R.V.) Belgica; a) general view of raw data soundings; b) N-S perspective view of raw data soundings; c) S-N perspective view of raw data soundings; d) lateral view of raw data soundings (modified and courtesy of Federal Public Service Economy, SMEs, independent Professions and Energy Service Continental shelf, Belgium).

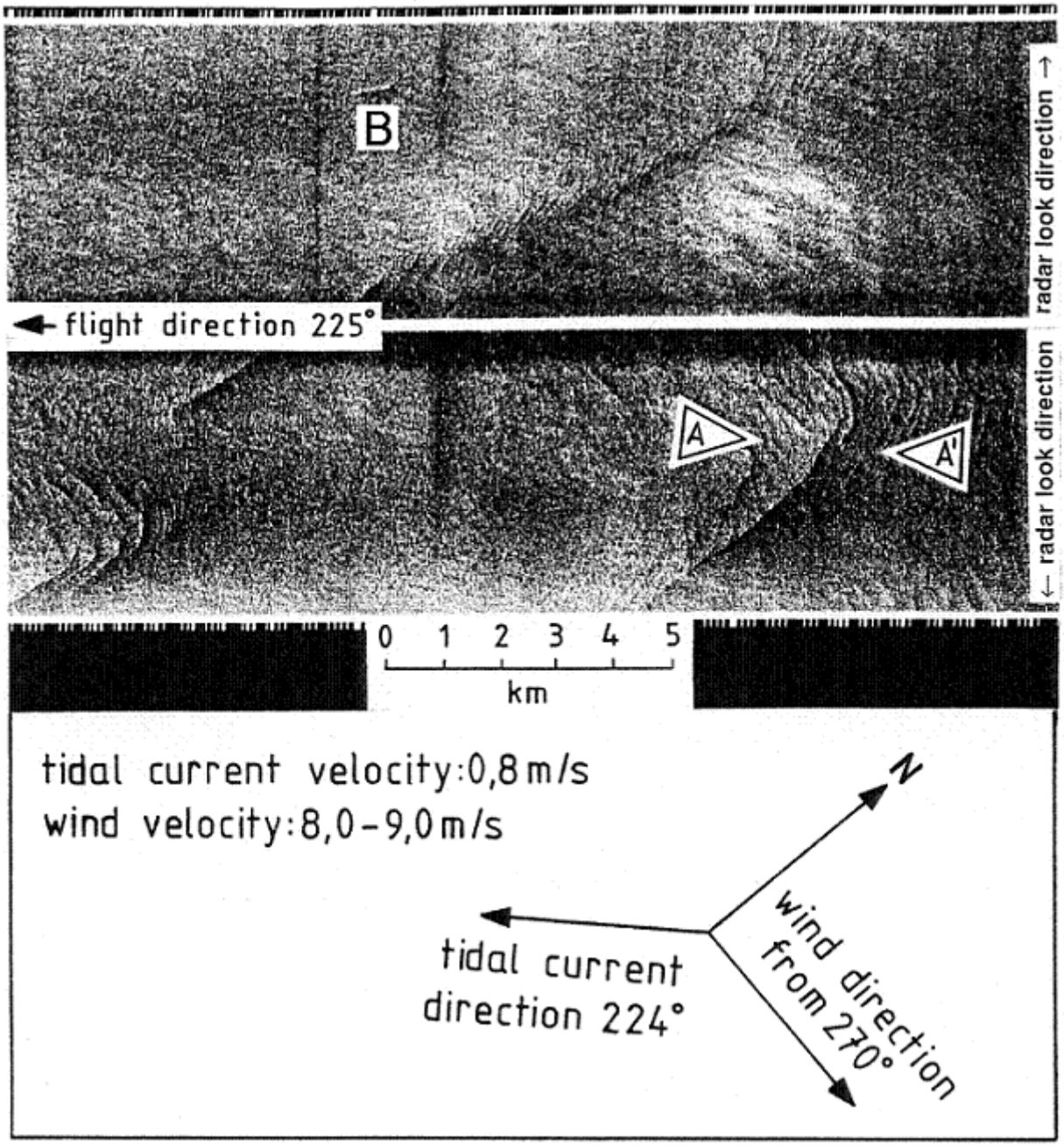

Figure 4: NOAA airborne APD-7 RAR K_a-band image acquired on 8 December 1979 11:30 UTC during ebb tidal current phase of the Hinder Banks in the southern North Sea. Sea bed signatures of the Hinder Banks are visible as well as signatures of marine sand waves are identified as sea surface manifestations. Local wind streaks are additional imaged radar signatures in the image. The radar signature of the M.V. Birkenfels wreck can be identified in the upper left section of the image marked by B.

attached to the bottom of the ship and is stretched out with a bar of about one meter from beneath the keel. Manifestations of two sand ribbons on both sides of the wreck with an angle of 25^0 in relation to the length scale of the wreck are shown in Figs. 3a-c. The height of the sand ribbons has been estimated between 2 m and 5 m, the maximum width of the ribbons is 35 m, the length of the ribbon is 85 m at the northern side and 160 m at the southern side, respectively.

Figure 4 is an airborne APD-7 real aperture radar (RAR) K_a-band image acquired on 8 December 1979 11:30 UTC from on board a Lockheed P-3D Orion aircraft of the National Oceanic and Atmospheric Administration (NOAA) during ebb tidal current phase with the position of an analyzed

radar image intensity profile A-A', which is not shown here. The radar signature of the M.V. Birkenfels wreck can be clearly identified in the upper left section of the image, marked by the capital letter B. This radar signature with a length of 760 m is imaged like a comet mark often visible on side-scan sonar records. The spatial resolution of the RAR image is 10 m in antenna look direction and 2 mrad in flight direction. Mean height of the radar platform above the sea surface was 1300 m, the RAR had a frequency of 34.85 GHz with a wavelength of 0.86 cm, the polarization was horizontal/horizontal (HH) for transmitting and receiving, respectively, and the radar incidence angle was between 10^0 and 80^0. Sea bed signatures of the Hinder Banks are visible in Fig. 4 as well as signatures of marine sand waves which turned out to be sea surface manifestations. Furthermore, local wind streaks are also imaged as bright radar signatures in Fig. 4. The aircraft flight direction, radar look directions to port and starboard sides of the aircraft flight direction, the mean wind direction, and the mean tidal current direction are also indicated in Fig. 4. The mean tidal current speed was 0.8 m s^{-1} and a wind speed between 8 m s^{-1} < U_w < 9 m s^{-1} has been observed. The mean wind direction was from 270^0 and the mean tidal current direction was 224^0 at the acquisition time of the RAR image.

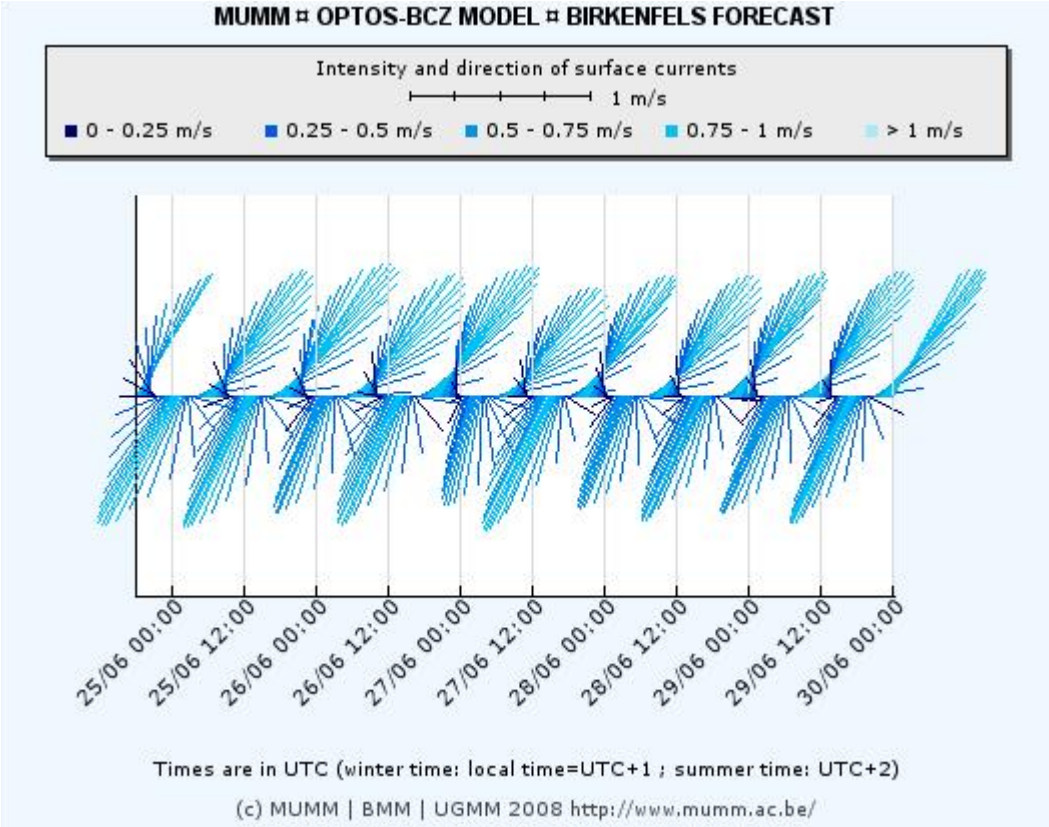

*Figure 5: Surface current intensities and –directions at the M.V. Birkenfels wreck position in the southern North Sea, calculated for the period of 24-30 June 2008, as an example (*http://www.mumm.ac.be*).*

To obtain any information on the behaviour of the current flow, routinely calculations of surface current intensities and –directions at the M.V. Birkenfels wreck position for the period of 24-30 June 2008 were used for example and are shown in Figure 5 (http://www.mumm.ac.be). For the same period, a maximum variation of the water surface elevation of about 2.80 m due to tidal current forces has been calculated by using hydrodynamic models (http://www.mumm.ac.be). It is evident from Figs. 3-5 that all three directions defined by: 1. the sand ribbons associated with the length scale of the wreck at the sea bed, 2. the associated orientation of the radar signature at the sea surface, and 3. the dominant current flow, respectively, coincide fairly well. It is assumed here that the shape, position and orientation of the wreck, the sand ribbons around the wreck and the

dominant peak tidal current velocity may have not changed significantly during the different long time periods between the observation events.

THEORY

A new view on the radar imaging mechanism of underwater wrecks is proposed applying the quasi-specular scattering theory of shallow sea bottom topography considering both, the gravity as well as the capillary wave ranges. It has been generally accepted by the scientific community that the radar imaging mechanism of underwater bottom topography can be physically and mathematically described as a process consisting of at least three steps (xi, xii): 1. The interaction between the (tidal) current and the sea bottom topography causing variable current velocities and creating alternating divergent and convergent zones at the sea surface. 2. The variation of the surface current modulates the short-scale sea surface roughness which is described by the weak hydrodynamic interaction theory in the relaxation time approximation. 3. The disturbed variance of slopes of short ocean surface waves via the modulation of the spectral wave energy density at the water-air boundary layer is the source for changes in radar backscatter.

Radar signatures of sea bottom topography are dominated by Bragg scattering since most of the imaging radars operate at incidence angles between 20° and 70° (xiii). At radar incidence angles less than 20° quasi-specular scattering is dominating. In addition, quasi-specular scattering becomes dominant at higher radar frequencies of about 9.5 GHz. According to Bragg scattering theory, the NRCS for small water surface waves is proportional to the wave height spectral density at the Bragg backscatter wave numbers. For quasi-specular scattering from a rough ocean surface, the NRCS is proportional to the total variance of slopes created by ocean surface waves. The radar imaging mechanism of sea bottom topography applying Bragg scattering depends strongly on radar incidence angle, radar frequency, radar polarization, current speed and -direction, as well as wind speed and -direction. The most important assumption for the radar imaging mechanism of submarine bed forms is the presence of strong currents, preferably tidal currents ≥ 0.5 m s^{-1} at wind speeds ≤ 8 m s^{-1}. Specular reflection arising when radiation is scattered into a given direction from surface regions with slopes such that the local specular direction coincides with the scattering direction. The quasi-specular scattering theory can be applied if the wavelengths of waves in the ocean contributing to the mean square surface slope are greater than the wavelength of the microwave.

Here, the quasi-specular scattering theory (xiv) for two different wind regimes is applied. The disturbed NRCS $\delta\sigma_{dis}$ caused by the disturbance of the surface current $\delta U(\mathbf{x})$, with $\mathbf{x}$ as the space variable, due to marine sand waves based on quasi-specular scattering and on a Gaussian distribution, respectively, is given by (xii)

$$\delta\sigma_{dis} = \sigma - \sigma_0 = \frac{|R(0)|^2}{\left(s_0^2 + \delta s^2\right)} \frac{1}{\cos^4(\theta_0 + \delta\theta)} \exp\left(-\frac{\tan^2(\theta_0 + \delta\theta)}{s_0^2 + \delta s^2}\right) - \sigma_0 \qquad (1)$$

where σ is the local NRCS influenced by the disturbance of $\delta U(\mathbf{x})$, σ_0 is the background NRCS, $R(0)$ is the Fresnel reflection coefficient at normal incidence, θ_0 is the angle of incidence, $\delta\theta$ is the time dependent perturbation term of the incidence angle, s_0^2 is the mean square slope, and δs^2 is the time-dependent disturbed square slope of water waves.

It has been shown (xv) that the mean square slope of sea surface waves can be obtained from the wave height spectrum $\psi(\mathbf{k})$ of ocean waves

$$s^2 = \int k^2 \psi(\mathbf{k}) \mathrm{d}\mathbf{k} \tag{2}$$

where $\mathbf{k}$ is the wave number vector and integrating in equation (ii) should cover the responsible range of wave numbers (see equations (ix)-(xi)). The relationship between $\psi(\mathbf{k})$, the wave-energy density spectrum $F(\mathbf{k})$ and the wave action density spectrum $N(\mathbf{k}) = F(\mathbf{k})\left(\omega'(k)\right)^{-1}$ is defined by (16)

$$F(\mathbf{k}) = \omega'(k) N(\mathbf{k}) = \frac{\omega'(k)^2}{k} \psi(\mathbf{k}) \tag{3}$$

where ω' is the intrinsic angular wave frequency defined by

$$\omega' = \left(gk + \frac{T}{\rho} k^3 \right)^{1/2} \tag{4}$$

where g denotes the acceleration of gravity, ρ and T are the density and the surface tension of water, respectively.

Equation (ii) can also be expressed for the equilibrium or saturation range like

$$s^2 = \int_{k_0}^{k_\gamma} k^2 \chi(\mathbf{k}) \mathrm{d}k \tag{5}$$

where k_0 is the wave number at the spectral maximum, and k_γ is the maximum wave number neglecting the influence of surface tension. The distribution $\chi(\mathbf{k})$ of the mean square surface wave displacement $\overline{\varsigma^2}$ among wave numbers, regardless of direction α, where the angle α specifies the direction of $\mathbf{k}$, is given by

$$\chi(\mathbf{k}) = \int_0^{2\pi} \psi(\mathbf{k}) k \mathrm{d}\alpha \tag{6}$$

with the wave height spectrum

$$\psi(k) = Bk^{-4} \tag{7}$$

in which B is a spectral coefficient to be determined.

The Phillips' spectrum as defined by equation (vii) is primarily applicable to the saturation range of short gravity waves. The saturation range denotes the quasi-steady state in which a delicate, and poorly understood, balance between wind-forcing, nonlinear interaction among different wave components and dissipation by wave breaking maintains a spectrum in which the energy density falls with the fourth power of the wave number (xvii). The saturation spectrum corresponds to a wave field which, statistically, shows spatial discontinuities in the slope, i.e., the first spatial derivative. This fact emphasizes that the slope is a basic parameter for the waves (xviii). From the experimental point of view, slope measurements offer a significant advantage to height measurements since the slope signal has a much smaller dynamic range.

In 1966, a spectrum of the same form has been suggested for the capillary range but with a spectral coefficient B' different from B (xv). It is noted that the Phillips' spectrum for gravity range has been supported by experimental observations while that for capillary range has not previously been verified. It has been demonstrated (xix) that the measured mean-square slope of the sea surface varying logarithmically with the wind velocity, and the rates of variation change with different boundary-layer regimes of the wind. Based on these data, the form of a newly proposed equilibrium wind-wave spectrum for capillary range has been verified (xix), the spectral coefficients for both gravity and capillary ranges, respectively, have been determined, and the cut-off wave number for the slope data was shown to be much smaller than the neutrally stable wave number obtained from laminar model.

Inserting equation (vii) into equation (vi) and then equation (vi) into equation (v), yields

$$\overline{s^2} = s_0^2 = B \int_{k_0}^{k_\gamma} k^{-1} \mathrm{d}k + B' \int_{k_\gamma}^{k_\nu} k^{-1} \mathrm{d}k \qquad \text{(viii)}$$

with

$$k_0 = \frac{g}{U_{10}^2} \qquad \text{(ix)}$$

$$k_\gamma = \left(\frac{g\rho}{T} \right)^{\frac{1}{2}} \qquad \text{(x)}$$

and

$$k_\nu = 1.67 \times 10^{-2} U_{10}^2 k_\gamma \qquad \text{(xi)}$$

where U_{10} is the wind velocity at standard anemometer height of 10 m. The first term on the right-hand side of equation (viii) represents the contribution of gravity waves, and the second term on the right-hand side is the contribution of capillary waves to the mean-square surface slope.

Equation (viii) can be rewritten like

$$s_0^2 = B \ln\left(\frac{k_\gamma U_{10}^2}{g}\right) + B' \ln\left(\frac{k_\nu}{k_\gamma}\right) \quad \text{(xii)}$$

where B has been found to be B = 4.6 x 10^{-3} and B' has been determined to be B' = 3.15 x 10^{-2}. The data analyzed by (xix) indicated that the mean-square slope is the contribution of wave components from the gravity range only at low to moderate wind velocities of $U_w \leq$ 7 m s^{-1}, and from both, gravity as well as capillary ranges, at high wind velocities of 7 m s^{-1} < $U_w \leq$ 15 m s^{-1}.

The square tangent of the disturbed incidence angle in equation (i) is defined by

$$\tan^2 \delta\theta = +\delta s^2, \quad \frac{\partial u_{perp}}{\partial x_{perp}} \leq 0 \quad \text{(xiiia)}$$

$$-\tan^2 \delta\theta = -\delta s^2, \quad \frac{\partial u_{perp}}{\partial x_{perp}} > 0 \quad \text{(xiiib)}$$

with the disturbed square slope

$$\delta s^2 = \int_{k_r}^{k_c} \mathbf{k}^2(\mathbf{x}) \delta\psi(\mathbf{x},\mathbf{k}) \mathrm{d}\mathbf{k} \quad \text{(xiv)}$$

where x_{perp} is the space variable defined perpendicular to the wreck mark or sand ribbon, k_r is the lower limit of the wave number producing quasi-specular scattering modulation, k_c is the maximum wave number where the quasi-specular scattering theory can be applied, i.e., the wavelengths of waves in the ocean contributing to the mean square surface slope have to be at least equal or greater than the wavelength of the microwave, $\partial u_{perp} / \partial x_{perp}$ is the gradient or strain rate of the current velocity perpendicular to the sand ribbon, and $\delta\psi(\mathbf{x},\mathbf{k})$ is the perturbation term of the wave-height spectrum in the short wave regime caused by wave-current interaction applying weak hydrodynamic interaction theory (xx). The perturbation term $\delta\psi(\mathbf{x},\mathbf{k})$ can be interpreted as the density of contributions to δs^2 per unit area in $\mathbf{k}$ -space.

A typical spatial scale of waves responsible for the quasi-specular scattering modulation assumed for K_a–band radar has to be in the range of wavelengths $\lambda_c = 2\pi / k_c = 0.0086$ m and $\lambda_r = 2\pi / k_r = 10$ m. These values have been selected because the K_a-band radar wavelength is $\lambda_r = 0.0086$ m and the spatial resolution of the radar is $\rho_{radar} = 10$ m. The parameters $\delta\theta$ and δs^2 expressed by equations (xiii)-(xiv) are defined positive as well as negative depending on the sign of the current gradient or strain rate $\partial u_{perp} / \partial x_{perp}$. Short surface waves are stretched within a divergent current regime and the square tangent of the local incidence angle and the total variance

of local slopes are reduced from equilibrium due to a diminishing wave height spectrum $\psi(\mathbf{k})$ or wave-energy density spectrum $F(\mathbf{k})$. On the other hand short surface waves are compressed within a convergent current regime, the square tangent of the local incidence angle and the total variance of local slopes are enhanced from equilibrium due to an increased wave height spectrum $\psi(\mathbf{k})$ or wave-energy density spectrum $F(\mathbf{k})$.

The modulation of the first order perturbed wave height spectrum is defined by $\delta\psi / \psi_0 = (\psi - \psi_0)/\psi_0$, with ψ_0 as the unperturbed wave height spectrum, which is proportional to the modulation of the wave-energy density spectrum (see equation (iii) for the relation between the local wave height and local wave-energy density spectrum). For the modulation of the first order perturbed wave-energy density spectrum $\delta F / F_0 = (F - F_0)/F_0$, with F_0 as the unperturbed wave-energy density spectrum, the following expression is used (xi)

$$\frac{\delta F}{F_0} = -(4+\gamma)\frac{\partial u_{perp}}{\partial x_{perp}}\left((\mathbf{c_g} + \mathbf{u_0})\frac{1}{L} + \mu\right)^{-1} \tag{xv}$$

with

$$\gamma = \frac{k}{\omega'}\mathbf{c_g} = \frac{k}{\omega'}\frac{\partial \omega'}{\partial k} = \frac{1}{2}\frac{g + 3\left(\frac{T}{\rho}\right)k^2}{\left(gk + \left(\frac{Tk^3}{\rho}\right)\right)^{\frac{1}{2}}} \tag{xvi}$$

where $\mathbf{c_g}$ is the group velocity of water waves, $\mathbf{u_0}$ is the mean current velocity of the undisturbed sea area, μ is the relaxation rate parameter, and L denotes the spatial scale of the residual flow cells.

Equation (xv) is derived by applying the action balance or radiation balance equation based on weak hydrodynamic interaction theory (xx). In this kind of transport equation the variation of the spectral energy density of short waves in a slowly varying current field is described. This implies that a slowly varying surface current is able to create only small magnitudes of the disturbed square slope. These conditions are often not fulfilled within a strong current gradient caused by large slopes of marine sand waves. On the other hand, according to the weak hydrodynamic interaction theory, it is sufficient that the strain rate has to be much less than the radian frequency of short surface water waves. This condition has been verified often during field experiments.

Transverse secondary circulation of flow over a rough sea bed is analogous to Langmuir circulation at the water surface due to wind stress. However, the dominant scale of such circulation may be responsible for low-relief sand ribbons in the presence of strong tidal currents. It has been assumed that helical secondary-flow circulations within a boundary layer are responsible for the lineation development such as sand ribbons and sedimentary furrows (xxi, xxii). Secondary circulations in the sea bottom boundary layer concentrate large, low-density particles in zones where there is flow convergence on the sediment surface. Thereupon, lineation such as sand ribbons can be formed. The schematic representation of the relationship between secondary circulations of the boundary layer, zones of convergence and divergence on the sea bed, sand ribbons, and sedimentary furrows in the model of furrow maintenance is presented in Figure 6 (xxii). It was shown

(xxiii) that inclusion of vertical flow structures turned out to be necessary to describe the formation, or absence, of all known large-scale regular sea bottom features. The residual component of the vertical velocity is one order of magnitude lesser than the horizontal residual velocity and is directed upward above the crests and downward towards the troughs. These residual flow components cause a residual circulation which favours the growth of the bed form, as shown in Figure 6. New in situ measurements show up- and down-welling phenomena of the three-dimensional current velocity field contributing significantly to the interaction between marine sand waves and the tidal flow, which has not been known before in detail (xxiv). The up- and down-welling regimes cause remarkable depressions at the troughs of sand waves with a maximum depth of 2 m and a width of up to 50 m. Similar circulation patterns associated with Langmuir super-cells off the coast of New Jersey of the eastern USA coast have been identified (xxv).

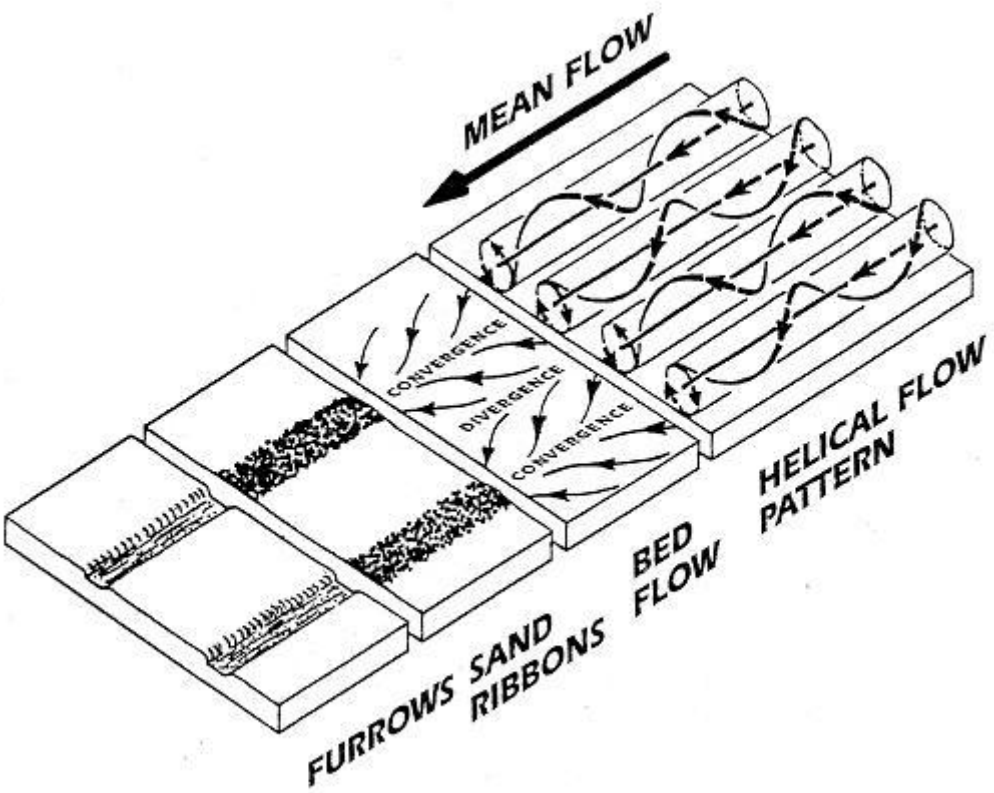

Figure 6: Schematic representation of the relationship between secondary circulations of the boundary layer, zones of convergence and divergence on the sea bed, sand ribbons, and sedimentary furrows in the model of furrow maintenance (xxii).

For the formation of the wreck mark such as a sand ribbon at the sea bed as shown in Fig. 3 and the manifestation of the associated radar signature at the water surface as imaged in Fig. 4 a vortex pair or helical flow cells are necessary to explain the wreck mark-(tidal) current-residual flow-water surface roughness interaction as a first approximation.

The divergence of a vector $\mathbf{v}$ is defined in cylinder coordinates by

$$\nabla \cdot \mathbf{v} = \frac{1}{\rho_{zyl}} \frac{\partial}{\partial \rho_{zyl}} \left(\rho_{zyl} v_{zyl} \right) + \frac{1}{\rho_{zyl}} \frac{\partial u_{\varphi_{zyl}}}{\partial \varphi_{zyl}} + \frac{\partial w}{\partial z_{zyl}} \qquad \text{(xvii)}$$

where ρ_{zyl} and φ_{zyl} are the polar coordinates of the projection of point P towards the main plain (usually x, y-plain), respectively, and z_{zyl} is the distance of point P from the main plain. If a tangential current of a spherical gyre is considered, $u_{\varphi_{zyl}}$ and $v_{\rho_{zyl}}$ of equation (xvii) are defined as

$$u_{\varphi_{zyl}} = U_0 \left(\frac{r}{h_0} \right) \exp - \left(\frac{r}{h_0} \right)^2 \tag{xviiia}$$

and

$$v_{\rho_{zyl}} = -\frac{U_0}{a} \left(\frac{r}{h_0} \right) \exp - \left(\frac{r}{h_0} \right)^2 \tag{xviiib}$$

where r is the radius of the gyre, h_0 is the water depth, U_0 is the magnitude of the local (tidal) current velocity, and a is an empirical constant which describes the ageostrophic behaviour of the residual flow circulation and has to be determined experimentally. The vortex current gradient according to equation (xvii) is then given by

$$\nabla \cdot \mathbf{v} = -\frac{2U_0}{ah_0} \exp - \left(\frac{r}{h_0} \right)^2 \cdot \left(1 - \frac{r^2}{h_0^2} \right) \tag{xix}$$

This second order circulation cell due to tidal current flowing over an obstacle such as a submarine wreck can then be approximated by the horizontal component of the tangential current gradient

$$\nabla \cdot \mathbf{v} = \frac{\partial v^h_{\rho_{zyl}}}{\partial x} = \cos\theta \frac{\partial v_{\rho_{zyl}}}{\partial \rho_{zyl}} \tag{xx}$$

where θ is the angle between the tangential current $\mathbf{v}$ and the horizontal component $\mathbf{v}^h$. As a first order approximation, the magnitude of $\partial v^h_{\rho_{zyl}} / \partial x$ as a function of water depth has been also used at the water surface for $\partial u_{perp} / \partial x_{perp}$ in equation (xv).

Figure 7 presents a schematic view of the unidirectional current flow direction, cross-structure residual flow above sand waves or sand ribbons (xxiii), the horizontal component of the tangential current of the secondary circulation cell $v^h(x)$ at the sea surface, the associated sea surface roughness and radar image intensity modulation due to accelerations and decelerations of the sea surface current velocity caused by the residual flow cell. The wind direction U_w is indicated by an arrow. In case if the wind direction is reversed then the other secondary circulation cell on the right hand side of the sand ribbon marked in Fig. 7 is responsible for the radar imaging mechanism of the wreck.

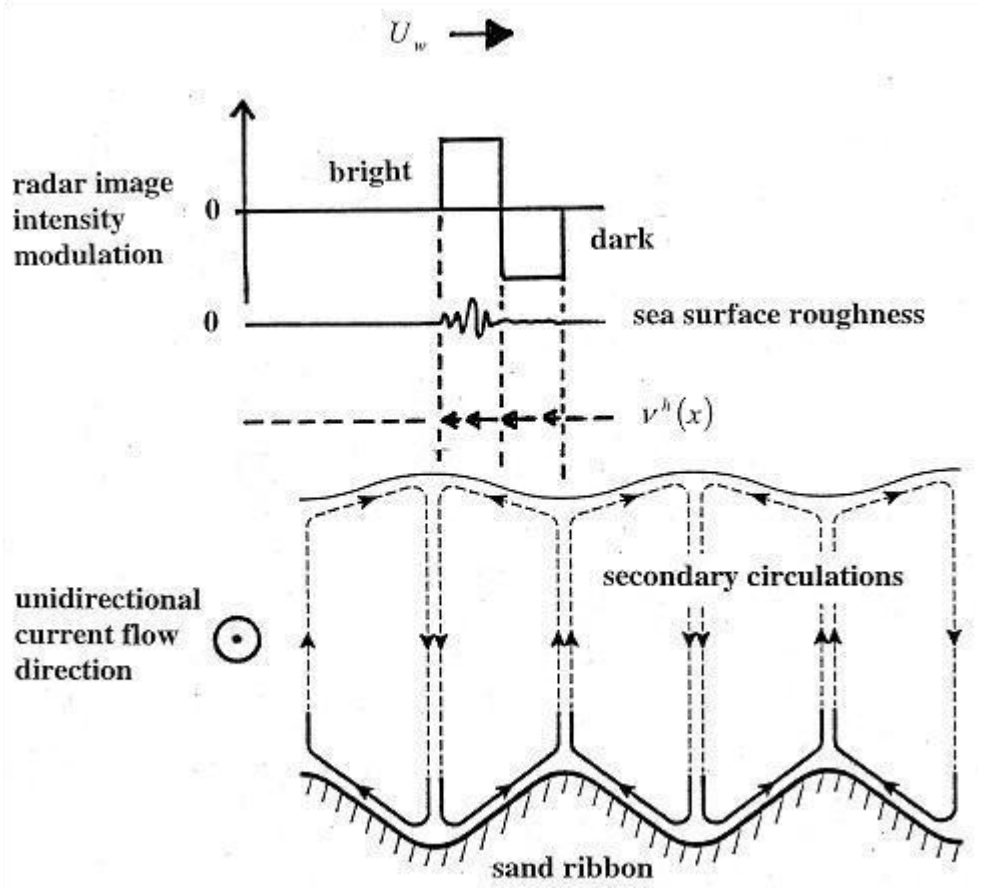

Figure 7: Schematic sketch of the unidirectional current flow (coming out of the graphic plane as has been observed in Figs. 4-5), cross-structure residual flow above sand waves or sand ribbons (xxiii), horizontal component of the tangential current of the secondary circulation cell $v^h(x)$ at the sea surface, associated sea surface roughness, and radar image intensity modulation due to accelerated and decelerated sea surface current velocities of the residual flow cell. The wind direction U_w is indicated by an arrow.

An order of magnitude estimate of the vortex current gradient at the M.V. Birkenfels wreck can be obtained if the following values for U_0 = 0.8 m s^{-1}, h_0 = 36 m, a = 0.5, and r = h_0/2 = 18 m are inserted in equation (xix), yields for the strain rate $\partial u_{perp} / \partial x_{perp}$ = -0.037 s^{-1}. This value has the same order of magnitude as has been calculated for strain rates of other bed forms such as marine sand waves, for example. This implies that the responsible hydrodynamic interaction can produce radar signatures of submarine wrecks and make them visible at the sea surface under the conditions described above.

DISCUSSION AND CONCLUSIONS

The presented theory is a first-order theory, describing the NRCS modulation in the gravity as well as in the capillary wave ranges due to spherical helical eddies behind an obstacle such as an underwater wreck. However, the quasi-specular scattering theory has to be tested by simulations of the NRCS modulation caused by wreck marks or sand ribbons and has to be compared with measured NRCS modulation data.

It is assumed that quasi-specular scattering becomes dominant at higher radar frequencies like K_a- and X-band. This implies that the NRCS for small water surface waves is proportional to the total variance of slopes created by ocean surface waves. It has been shown (xix) that the mean square slopes of the sea surface are varying with the wind speed logarithmically and not linearly. The Phil-

lips' wave number spectrum of capillary waves in the equilibrium range has been herein verified. It was also shown (xix) that the correlation of the surface roughness height with the mean square slope further indicated that the growth of small waves is mainly due to the direct action of the wind. Of course, the relaxation rate μ is one of the most crucial parameters in weak hydrodynamic interaction theory and has to be taken into consideration applying the presented theory. Comprehensive discussions concerning μ have been published (xxvi, xxvii). It has also to be noticed here that the time-dependent perturbation terms caused by the disturbance of the surface current $\delta U(\mathbf{x})$ due to perturbations at the sea bed such as underwater wrecks obey also a Gaussian distribution which has not been verified until now.

Based on the wreck data, proposed theory, and discussion, the following conclusions can be made:

1. In general, the detection of radar signatures of wrecks can support rapid wreck search of hydrographical agencies of shallow sea areas to ensure the safety of shipping.

2. Wreck marks or sand ribbons as well as radar signatures of wrecks are indicators of the local (tidal) current direction.

3. Radar signatures of wrecks are indicators of helical flow cells triggered by unidirectional (tidal) current flow caused by the wreck lying on the sea bed.

4. The bright edge of an imaged radar wreck signature correlates with the windward direction.

5. Radar signatures of underwater wrecks look like comet marks as imaged on side scan sonar records.

6. Radar signatures of underwater wrecks depend on radar parameters, size and shape of the wreck, orientation of the wreck relative to the dominant (tidal) current velocity, surrounding water depth, water depth above the wreck, and local wind and current conditions.

ACKNOWLEDGEMENTS

The Federal Public Service Economy, SMEs, independent Professions and Energy Service Continental shelf, Belgium, is gratefully acknowledged for providing the multi-beam echo sounder images of the M.V. Birkenfels wreck. The Management Unit of the North Sea Mathematical Models (MUMM), Department VI of the Royal Belgian Institute of Natural Sciences, Brussels and Oostende, Belgium, is gratefully acknowledged for providing the iterative calculations of the intensity and direction of surface currents at the M.V. Birkenfels wreck position. D. B. Ross and M. Metzner are gratefully acknowledged for providing the K_a-band RAR image and for technical support, respectively.

REFERENCES

i Tamura, H, T Waseda & Y Miyazawa, 2009. Freakish sea state and swell-windsea coupling: Numerical study of the Suwa-Maru incident. Geophysical Research Letters, 36: L01607, doi: 10.1029/2008GL036280

ii Toffoli, A, J M Lefevre, E Bitner-Gregersen & J Monbaliu, 2005. Towards the identification of warning criteria: Analysis of a ship accident data base. Applied Ocean Research, 27: 281-291

iii Caston G F, 1981. Potential gain and loss of sand by some sand banks in the Southern Bight of the North Sea. Marine Geology, 41: 239-250

iv Van Riet J A, J Kaspers & B Buis, 1985. Safety standards for a 22-metre deep-draught route. The Journal of Navigation, 38: 91-113

v McLeish W, D J P Swift, R B Long, D Ross & G Merrill, 1981. Ocean surface patterns above sea-floor bedforms as recorded by radar, southern bight of North Sea. Marine Geology, 43: M1-M8

vi Hennings I, 2002. On the use of radar imagery for coastal sea bed changes and its potential in identifying submerged hazards. In: Observing our environment from space – New solutions for a new millennium, edited by G Begni (A A Balkema Publishers, Lisse), 57-64

vii Werner F, G Unsöld, B Koopmann & A Stefanon, 1980. Field observations and flume experiments on the nature of comet marks. Sedimentary Geology, 26: 233-262

viii Caston G F, 1979. Wreck marks: indicators of net sand transport. Marine Geology, 33: 193-204

ix Ward J A K, P Larcombe & P Veth, 1999. A new process-based model for wreck site formation. Journal of Archaeological Science, 26: 561-570

x Quinn R, 2006. The role of scour in shipwreck site formation processes and the preservation of wreck-associated scour signatures in the sedimentary record – evidence from seabed and sub-surface data. Journal of Archaeological Science, 33: 1419-1432

xi Alpers W & I Hennings, 1984. A theory of the imaging mechanism of underwater bottom topography by real and synthetic aperture radar. Journal of Geophysical Research, 89(C6): 10529-10546

xii Hennings I & D Herbers, 2006. Radar imaging mechanism of marine sand waves at very low grazing angle illumination caused by unique hydrodynamic interactions. Journal of Geophysical Research, 111: C10008, doi: 10.1029/2005JC003302

xiii Valenzuela G R, 1978. Theories for the interaction of electromagnetic and ocean waves-A review. Boundary Layer Meteorology, 13: 277-293

xiv Barrick D E, 1968. Rough surface scattering based on the specular point theory. IEEE Transactions on Antennas and Propagation, AP-16: 449-454

xv Phillips O M, 1977. The Dynamics of the Upper Ocean (Cambridge University Press) 336 pp.

xvi Holliday D, G St-Cyr & N E Woods, 1986. A radar ocean imaging model for small to moderate incidence angles. International Journal of Remote Sensing, 7: 1809-1834

xvii Phillips O M, 1958. The equilibrium range in the spectrum of wind-generated waves. Journal of Fluid Mechanics, 4: 426-434

xviii Jähne B & K S Riemer, 1990. Two-dimensional wave number spectra of small-scale water surface waves. Journal of Geophysical Research, 95(C6): 11531-11546

xix Wu J, 1972. Sea-surface slope and equilibrium wind-wave spectra. The Physics of Fluids, 15: 741-747

xx Alpers W & K Hasselmann, 1978. The two-frequency microwave technique for measuring ocean wave spectra from an airplane or satellite. Boundary Layer Meteorology, 13: 215-230

xxi Karl H A, 1980. Speculations on processes responsible for mesoscale current lineations on the continental shelf, southern California. Marine Geology, 34: M9-M18

xxii Viekman B E, R D Flood, M Wimbush, M Faghri, Y Asako & J C Van Leer, 1992. Sedimentary furrows and organized flow structure: A study in Lake Superior. Limnology and Oceanography, 37: 797-812

xxiii Hulscher J M H, 1996. Tidal-induced large-scale regular bed form patterns in a three-dimensional shallow water model. Journal of Geophysical Research, 101(C9): 20727-20744

xxiv Hennings I, D Herbers, K Prinz & F Ziemer, 2004. First results of the OROMA experiment in the Lister Tief of the German Bight in the North Sea. EARSeL eProceedings, 3: 86-104

xxv Gargett A, J Wells, A E Tejada-Martinez & C E Grosch, 2004. Langmuir supercells: a mechanism for sediment resuspension and transport in shallow seas. Science, 306: 1925-1928

xxvi Caponi E A, D R Crawford, H C Yuen & P G Saffman, 1988. Modulation of radar backscatter from the ocean by a variable surface current. Journal of Geophysical Research, 93(C6): 12249-12263

xxvii Hennings I, B Lurin & N Didden, 2001. Radar imaging mechanism of the sea bed: Results of the C-STAR experiment in 1996 with special emphasis on the relaxation rate of short waves due to current variations. Journal of Physical Oceanography, 31: 1807-1827

http://www.bsh.de. Bundesamt für Seeschifffahrt und Hydrographie, Meeresdaten, Seevermessung und Wracksuche, 2007. Accessed 31.01.2007

http://www.ddg-hansa.de. Deutsche Dampfschifffahrts-Gesellschaft „Hansa“, Die Frachter, Technische Daten, 2008. Accessed 06.11.2008

http://www.mumm.ac.de. Management Unit of the North Sea Mathematical Models (MUMM), Department VI of the Royal Belgian Institute of Natural Sciences, MUMM, MODELS, OPERATIONAL, CURRENTS, EVOLUTION IN TIME AT BIRKENFELS, Forecast of the surface current at Birkenfels, 2008.